Conditions and mechanism for the formation of iron-rich Montmorillonite in deep sea sediments (Costa Rica margin): Coupling high resolution mineralogical characterization and geochemical modeling

Delphine Charpentier, Martine Buatier, Emmanuel Jacquot, Anne Gaudin, Geoffery C. Wheat

Conditions and mechanism for the formation of iron-rich Montmorillonite in deep sea sediments (Costa Rica Margin): Coupling high resolution mineralogical characterization and geochemical modeling

D. Charpentier[1*], M.D. Buatier[1], E. Jacquot[2], A. Gaudin[3] and C. G. Wheat[4]

[1] CNRS-Université de Franche-Comté/UMR 6249 Chrono-environnement, Université de Franche-Comté, 16, route de Gray F-25065 Besançon, France

[2] GEOKEMEX, 18 rue Alain Savary, 25000 Besançon, France

[3] LPGN UMR-CNRS 6112, Faculté des Sciences et des Techniques, 2 rue de la Houssinière 44 322 Nantes

[4] Global Undersea Research Unit, P. O. Box 475, Moss Landing, CA 95039, USA

* Corresponding author:

e-mail address: delphine.charpentier@univ-fcomte.fr

Fax number : 33 (0)3 81 66 65 58

Abstract

Iron-rich smectite is commonly described in the diagenetic fraction of deep-sea sediment, as millimeter to centimeter aggregates dispersed in the sediment, or as a coating on sedimentary particles or nodules. This study examines several factors to elucidate formation mechanisms of a particular iron-rich smectite and its potential transformation to glauconite. The study combines a detailed mineralogical investigation on natural samples and a chemical modeling approach to assess mineralogical reactions and pathways.

Transmission electron microscopy (TEM) observations and analytical electron microscopy (TEM–AEM) analyses were conducted on microtomed samples of millimeter- to centimeter-long green grains. These grains are widespread in pelagic calcareous sediment from the Costa Rica margin. They are composed of pyrites that are partially dissolved and are surrounded by amorphous or very poorly crystallized iron-rich particles. Iron-rich montmorillonite grows from an amorphous precursor and its formation requires the input of Si, O, Mg, K, Na and Ca; our results suggest that these inputs are supported by the dissolution of sedimentary phases such as volcanic glasses, siliceous fossils and silicates.

Thermodynamic modeling of fluid-sediment interactions was conducted with the geochemical computer code PhreeqC, using mineralogical and pore fluid compositions from sediment samples and calculated estimates for thermodynamic constants of smectites that are not maintained by the computer code. Simulations confirm the possibility that the green grains are the product of pyrite alteration by seawater under oxidizing conditions. The extent of smectite production is controlled by the kinetics of pyrite dissolution and fluid migration. The absence of aluminum in the Costa Rica margin system explains the formation of an iron-rich montmorillonite instead of glauconite, whereas the presence of calcite that buffers the system explains the formation of an iron-rich montmorillonite instead of iron oxides.

1. INTRODUCTION

Iron-rich smectites, (e.g., nontronite, saponite and montmorillonite) are common authigenic minerals in marine sediment, consisting of Fe-smectite and Mn and Fe oxi/hydroxides components dispersed in the sediment matrix, or as a coating on sedimentary particles or nodules (Chen et al., 1996). Nontronite and montmorillonite are dioctahedral smectites with a relatively high layer charge that is generated by tetrahedral substitution in nontronite and by octahedral substitution in montmorillonite. Saponite can be iron- or magnesium-rich and has a trioctahedral structure. Each of these minerals forms naturally in oceanic sediments, but with different environmental conditions.

In general, the glauconitization process, thought to occur via diffusive transport of dissolved ions in pore waters, leads to the precipitation of iron-rich smectite (nontronite or montmorillonite) as glauconite precursor (in Meunier, 2003). Furthermore, glauconite (mixture of Fe- and Al-rich smectite and mica) is a common clay mineral associated with early diagenetic process generally described in the outer part of the continental shelf sediment (Odin and Matter, 1981; Odin and Morton, 1988), but can form in the deep sea (e.g., Giresse and Wiewora, 2001; Wiéwiora et al., 2001).

The presence of nontronite in marine sediment is generally attributed to a hydrothermal origin. Nontronite deposits have been described with sulphur deposits near active high temperature black and white smokers (Bischoff, 1972; Thompson et al., 1985; Köhler et al., 1994), but also in lower temperature off-axis hydrothermal systems (Corliss et al., 1978; Moorby and Cronan, 1983). The formation of these nontronite deposits occurs at temperatures <70°C, where hydrothermal fluids mix with sea water (Singer et al., 1984). Nontronite has long been considered the most abundant authigenic smectite in recent marine sediments (Cole and Shaw, 1983).

In contrast, iron-rich montmorillonite is believed to be the rarest of these three iron-rich

smectites. However, this conclusion may be an analytical artifact. For example, most mineralogical and chemical investigations on iron-rich clays cited above are based on bulk wet chemical analyses or microprobe analyses. Such tests were conducted on an Fe(III)-rich deposit from the Galapagos hydrothermal mounds where biogenic calcareous sediment alternates with iron-rich clays. Initially these deposits were described as nontronite, based on bulk wet chemical analyses (Corliss et al., 1978; Moorby and Cronan, 1983), but these methods do not allow accurate characterization of the clay mineral structure. A detailed crystallochemical characterization using TEM-AEM (transmission analytical electron microscopy) analyses and Mossbauer spectroscopy was conducted on these Fe(III)-rich clays, revealing the presence of iron-rich montmorillonite and goethite (Buatier et al., 1989, 1993). Furthermore, montmorillonite and saponite assemblages have been described as products of sediment alteration by a low temperature (<60°C) hydrothermal fluid on the flank of the Juan de Fuca ridge (Buatier et al., 2002). The successive formation of montmorillonite and saponite is attributed to oxido-reduction conditions; saponite requires more reducing conditions.

The presence of iron-rich montmorillonite in oceanic environments suggests that the mineral forms at low temperature (less than 70 °C) in an oxygenated environment, but the mechanism of formation is still not fully understood. This study focuses on the mechanism that formed millimeter to centimeter-sized green grains of iron-rich montmorillonite along the Costa Rica margin (Gaudin et al., 2005). Sediment samples were taken from dominantly pelagic carbonates with widespread green grains located in the upper bioturbated zone. Green grains correspond to burrows that included pyrite, suggesting an early diagenetic origin. After Gaudin et al. (2005), each grain is concentrically microlaminated. The central zone of the burrow is composed of framboidal pyrite crystals whereas the outer zone is composed of a clay coating and strongly dissolved pyrite grains. An intermediate zone with partially dissolved pyrite surrounded by newly formed smectite and Fe-oxide were identified. Clays display the typical honeycomb structure commonly found for authigenic smectite and the average clay composition is $[Si_{3.94}\ Al_{0.04}\ Fe_{0.02}\ O_{10}]\ (Fe_{1.42}\ Mg_{0.68}\ Mn_{0.02})\ (K_{0.11}\ Ca_{0.11}\ Na_{0.07}\ nH_2O)\ (OH)_2$. Here we extend this study to elucidate the formation

mechanism and conditions of this iron-rich montmorillonite using TEM (Transmission electron microscopy) analysis and a chemical modeling approach. These activities constrain which parameters are essential for the precipitation and stability of iron-rich montmorillonite in a deep-sea environment.

2. MINERALOGICAL APPROACH

2.1. Samples

Sediment cores were recovered at a water depth of 3000 m during the Ticoflux II expedition in 2002, offshore of the Nicoya Peninsula on the Costa Rica Margin (Fig. 1). Results from ODP Leg 170 in this area (ODP Site 1039) indicate a sediment thickness of ~450 m (Silver et al., 2001). The upper 150 m is composed of hemipelagic mudstones (Pliocene and Pleistocene in age). The lower section (under 150m) is made of calcareous pelagic nanofossil oozes (Miocene). The calcareous nanofossil ooze (a non-indurated chalk) is composed of an assemblage of coccoliths with sponge spicules, diatoms and radiolarian fossil remains. Spinnelli and Underwood (2004) characterized the sediment mineralogy and their spatial variability along the Costa Rica margin. They used alkaline leaching methods to quantify the opal content and XRD analyses to determine the bulk mineralogy. The composition of calcareous ooze is 3 wt% opal, 4 wt% quartz, 4 wt% plagioclase and 88.5 wt% calcite with less than 1 wt% smectite, gypsum and barite. The porosity of the calcareous nanofossil ooze determined by Kimura et al. (1997) is about 50-60 %.

Millimeter to centimeter green grains showing a burrow form described by Gaudin et al. (2005) were recovered in gravity cores 22GC, 27GC, 28GC and 31GC (Fig. 1). On the basis of seismic data collected during the Ticoflux expedition, sediment thicknesses in the area where these cores were recovered are less than 100 m in close proximity to a hydrologically active off-axis seamount (Wheat and Fisher, 2008). Sediment from these cores is dominated by calcareous oozes

with coccoliths and siliceous fossil remains (Fig.2a). An initial analysis of these sediments was conducted by Gaudin et al. (2005) and outlined below for completeness. XRD analyses indicate that the sediment surrounding the green grains contains barite associated with carbonate and siliceous fossil remains, but is void of feldspar. A concentric zoning exists with a black core consisting of octahedral pyrites that are about 0.2-2 µm wide, the green rim is composed of smectites (Fig.2b), which progressively replace pyrite grains. On Fig. 2c, patterns of air-dried preparations show an intense 001 reflection near 14.6 Å, after heating to 390°C the 001 reflection collapsed to 9.70 Å, and after ethylene glycol saturation the 001 reflection shifted to 16.9 Å. These data are characteristic of smectite without non-swelling interlayer. XRD analyses performed by Gaudin et al. (2005) also show patterns of randomly oriented powders of smectite exhibiting asymmetrical (hk) reflections near 4.5 and 2.5 Å, indicative of a turbostratic stacking layer; and unusual (06-33) reflection at 1.513 Å characteristic of Fe^{3+}, Mg-rich dioctahedral smectites. They also performed AEM analyses on particles of smectite after Ca^{2+}-saturation or in the natural state of saturation. Both the individual particle and the average structural formulae were calculated for O_{10} $(OH)_2$, with total iron in the ferric state (as expected from the XRD d(06-33) values and the IR data) and Mg in the octahedral sheets of smectite layers (as expected from Ca^{2+}- saturation). Plotted in the 4Si – ΣFe^{VI} diagram modified from Meunier *et al.* (2003), the chemical compositions of the smectite are grouped in the iron-rich montmorillonite domain (Fe-rich smectite with a dominant octahedral charge) (Fig. 2d).

2.2. Methods

2.2.1. Pore water chemical analysis

Sediment pore water was extracted from split gravity cores. Sediment that was not affected by smearing along the edge of the core liner was placed into centrifuge tubes. For selected sediment

samples, this process was conducted within a nitrogen-filled glove bag. Samples were then cooled to 1-4°C, and spun for five minutes at ~11,000 rpm using a rotor head that was precooled to –20°C so that samples did not warm during centrifugation. Pore waters recovered after centrifugation were filtered through 0.45 μm filters and stored in a variety of acid-washed plastic and glass containers for ship and shore-based analyses. Some aliquots were acidified with subboiled 6N HCl.

Shipboard analyses used ion selective electrodes (pH), potentiometric titration (alkalinity and chlorinity), and colorimetric (phosphate) techniques. Shore-based analysis included inductively coupled plasma (ICP) emission spectrometry, ion chromatography, colorimetric, and mass spectrometric techniques (e.g., Wheat and Fisher, 2008).

2.2.2. Transmission electron microscopy (TEM)

Fragments of green grains were impregnated following the procedure established by Tessier (1984) and Elsass et al. (1988) for TEM analysis. This procedure consists of progressive exchange of the interstitial water with alcohol, solvent and then spurr resin. Ultrathin sections were obtained by ultramicrotomy using a diamond knife. Observations and EDX analyses were made on a TEM Philips CM30 at 300kV equipped with an EDAX Be detector (CCM, University of Lille 1). EDX measurements were made in STEM mode using a square window of about 10 nm. K factors were obtained from the analyses of standard minerals for each element relative to Si (natural andalusite for Al, natural jadeite for Na, natural wollastonite for Ca, synthetic pure forsterite for Mg and synthetic pure fayalite for Fe).

2.3. Results

A portion of the sediment pore water data is shown in Fig. 3. Depth profiles are homogeneous with compositions similar to that of bottom seawater. From these data we calculated

a “mean pore water” (Table 1, Fluid 1) and used this composition in modeling efforts.

TEM investigation allows one to examine the micro-scale transition from pyrite to iron-rich montmorillonite. TEM investigation of the center of the green grains shows a burrow form, demonstrating that pyrite is partially dissolved. On micrographs (Fig. 4a and b), we can see that the black partially dissolved pyrites are surrounded by aggregates of nano-sized particles. Electron diffraction patterns obtained on these aggregates show the absence of reflections around the transmitted beam, indicating that these particles are amorphous or poorly crystallized. These amorphous phases are also in contact with clay particles (Fig. 4c). Electron diffraction patterns obtained on the clay particles display two diffraction rings, respectively at 4.5 and 2.6 Å, corresponding to {hk0} reflections of typical turbostratic stacking layers of smectite particles (Fig. 4c). In Fig. 4d, amorphous particles are localized between pyrites and smectite particles composed of only two or three staking layers. Smectite layers are thicker with more than 10 layers in the outer portion of several green grains.

EDX analyses were carried out on three different phases: pyrite, amorphous particles and smectite along a transect. Fig. 5 shows the variation in composition along a transect from pyrite to secondary phases. This transect illustrates that the transition from pyrite (analyse n°1) to the amorphous phase (analyse n°2) results in an abrupt decrease in S and an input of Si and O, consistent with smectite formation (analyse n°5) that is characterized by an increase in Si, O and alkali elements and a decrease in Fe. The smectite composition of these samples is consistent with the average structural formulae for smectite established by Gaudin et al. (2005): $[Si_{3.94}\ Al_{0.04}\ Fe_{0.02}\ O_{10}]\ (Fe_{1.42}\ Mg_{0.68}\ Mn_{0.02})\ (K_{0.11}\ Ca_{0.11}\ Na_{0.07}\ nH_2O)\ (OH)_2$.

3. MODELING APPROACH

3.1. Methodology

The thermodynamic validity of suspected reactions was performed using version 2.15 of the computer program PhreeqC (Parkhurst, 1995; Parkhurst and Appello, 1999) in the context of a numerical model that includes reactive transport. PhreeqC was used to perform speciation, mineral saturation index calculations with respect to the solution, equilibrium, and batch reactions. Reactions included aqueous and mineral phases. The most concentrated fluid to be simulated is seawater, with an ionic strength of 0.7. Such fluids have been reasonably represented in numerical simulations using the extended Debye-Hückel expression for estimating activity coefficient values. We used the database Llnl.dat, which is derived from the EQ3/6 database (Wolery, 1992; Wolery and Daveler, 1992). This thermodynamic database does not contain iron-rich smectite, but it does include a few smectites end members. Because of this lack of data we added calculated thermodynamic constants for 18 additional smectites and one glauconite, using the method developed by Chermak and Rimstidt (1989, 1990). This large number of smectites was introduced so that the calculations would not bias which minerals were stable in this environment. Each smectite was decomposed into oxide and hydroxide components with a specific molal Gibbs energy (ΔG) (Table 2). Table 3 reports the composition, ΔG of formation (sum of composing oxi/hydroxide molal Gibbs energy of formation), ΔG of reaction (sum of ΔG for the formation of clay minerals, using aqueous species from SUPCRT92, Johnson et al. (1992)) and log K of smectites and glauconite that were added to the database. Thermodynamic equilibrium constants were calculated at 5°C. Glauconite was used as a single phase, whereas smectites were presented as end-members of a solid solution.

These thermodynamic calculations were then combined with a numerical mode to account for reactive transport. The conceptual model was a one-dimensional diffusion approach. In sediments with a high water/sediment ratio (W/R= 1), aqueous components are transported by diffusion. This is consistent with the lack of evidence for advective pore water circulation through these cores. In the pyrite-rich area, the fluid composition is controlled by the oxidation of pyrite from dissolved O_2 in seawater. Because pyrite is not in thermodynamic equilibrium, we introduced

kinetic parameters to simulate its oxidation. Pyrite oxidation by oxygen is generally described by the global reaction (Panin et al., 1985):

$2FeS_2 + 7.5O_2 + H_2O \rightarrow 2Fe^{3+} + 4SO_4^{2-} + 2H^+$ (reaction 1).

This global reaction is achieved by the following initial reaction,

$FeS_2 + 3.5O_2 + H_2O \rightarrow Fe^{2+} + 2SO_4^{2-} + 2H^+$ (reaction 2)

followed by, (Sévèque, 1986)

$Fe^{2+} + 0.25O_2 + H^+ \rightarrow Fe^{3+} + 0.5H_2O$ (reaction3),

Pyrite also can be oxidized by Fe^{3+} (Garrels and Thompson, 1960):

$FeS_2 + 14Fe^{3+}\ 8H_2O \rightarrow 15Fe^{2+} + 2SO_4^{2-} + 16H^+$ (reaction 4).

Given the mineralogy and pore water composition of the system, the oxidation of pyrite by Fe^{3+} was neglected in model simulations. In carbonate-rich environments, free Fe^{3+} is not present at significant concentrations in solution. In this environment free Fe^{3+} combines with dissolved carbonates at pH 6 or greater and with oxi/hydroxide minerals (Stefánsson et al., 2005; Sánchez España, 2007). The following rate equation (Williamson and Rimstidt, 1994) was adopted to model kinetic dissolution of pyrite:

$R=(1-Q)10^{-8.19}m_{O2}{}^{0.5}m_{H+}{}^{-0.11}$ (equation 1),

where R is the reaction rate ($mol.m^{-2}.s^{-1}$), Q is the saturation state, and m is the molality of a particular chemical species. Within the sediment, initial phase equilibria are affected by the acidification resulting from the oxidation of pyrite. Therefore, the rate of pyrite oxidation drives the overall transformation of the sediment. Under such conditions, there is no need to introduce the kinetic parameters for minerals other than pyrite, and dissolution and precipitation reactions in the sediment are assumed to take place based on the assumption of local equilibrium, using thermodynamic data as described previously. Smectites were here introduced as different clay phases.

3.2. Simulations

3.2.1. Origin of interstitial fluid

The first simulation focused on the nature of the pore fluid composition. Starting with the composition of seawater (Table 1, Fluid 2), we calculated a pore water composition that is in equilibrium with local sediment (72 wt% calcite, 22 wt% opal and 6 wt% barite (deduced from Gaudin et al. (2005)) and compared the calculated result with the mean pore fluid. Initial conditions set pCO_2 and pO_2 to values in seawater at 3000 mbsf and a temperature of 5°C (Chester (2000); $pCO_2 = 10^{-3.48}$atm, $pO_2 = 10^{-1.65}$atm). For seawater to reach equilibrium at these conditions, small quantities of calcite and amorphous silica (SiO_2(am)) need to dissolve, 7.9 10^{-5}mol/l and 9.5 10^{-4}mol/l, respectively, and 1.7 10^{-8}mol/l of barite will precipitate. The composition of the pore fluid resulting from the equilibration of seawater with sediment (Table 1, Fluid 3) approximates closely the measured composition of the pore fluid. Major element concentrations (Ca, Na, Mg, K, Cl, S) are equivalent; however, significant differences are observed for some trace elements. For example, iron concentrations are high in interstitial fluid relative to the calculated fluid. This high iron is likely a product of microbial reactions that are not included in the model(reference?). Thus, the pore fluid is one that is in equilibrium with sediment at low temperature.

3.2.2. Local smectite formation in green grains

In the pyrite-rich area, the fluid composition is controlled by the oxidation of pyrite with dissolved O_2 in seawater. We developed a simulation to ascertain whether commonly found minerals in carbonate settings (hematite, goethite, magnetite, gypsum, anhydrite, celestite and jarosite) should be produced during this pyrite oxidation. The objective was to define the role of silicates and clay minerals that constitute part of the matrix surrounding altered pyrite in Costa Rica

margin sediment. The interaction of pore fluid with sediment that contains pyrite under oxidizing conditions was numerically simulated by batch reactions. The initial solution was the mean composition of the pore fluid data (Table 1, Fluid 1) with $pO_2 = 10^{-1.65}$atm (corresponding to O_2 in seawater at 3000 mbsf after Chester, 2000), and a temperature of 5°C. The sediment composition is supposed to be about 72 wt% calcite, 22 wt% opal and 6 wt% barite, with an in situ sediment matrix that is 50% sediment and 50% interstitial fluid. With these initial conditions we calculate the possibility that iron oxi/hydroxides (hematite, goethite, magnetite), sulfates (gypsum, anhydrite, celestite and jarosite), or clay minerals (smectite, illite, muscovite, daphnite, clinochlore and glauconite) will precipitate and predict which smectitic solid-solutions (end-members described Table3) will exist.

The interaction of pore water with sediment and pyrite results in a change in the redox state from oxic to anoxic. The acidic fluid produced by pyrite alteration was buffered by the dissolution of calcite (Fig. 6): the pH of the solution decreased from 7.7 to 7.4. Smectite calculated as a solid-solution was the only by-product predicted from this simulation. The newly formed smectite has the following composition: $[Si_4\ O_{10}]\ (Fe_{1.4}\ Mg_{0.6})\ (Na_{0.3}\ K_{0.1}\ Ca_{0.1})\ (OH)_2$. This calculated composition is similar to the measured structural formulae; in both cases an iron-rich and aluminium-free montmorillonite exists.

3.2.3. Extent of Alteration

The extent of pyrite oxidation within the sediment was numerically simulated using a one-dimensional diffusion model in which oxidation occurs for 4000 years. The first cell was 5 mm in width. In this cell, pyrite could dissolve following the dissolution rate law described above. Pyrite is represented as a coating within a burrow described as a cylinder that is 3.2 cm in length and 0.6 cm in diameter. This corresponds to a pyrite reactive surface area of 167 cm^2/mol. The amount of reacting pyrite is 8.3 mol per kilogram of fluid. The next 200 cells represented the sediment, with

widths that range from 10 mm to 200 m for the last cell. Cell widths increase progressively from the burrow to the sediment to focus on the close proximity of the pyrite and to simulate an infinite media with respect to the pyritic burrow size (i.e., a constant boundary condition). As with the calculation above, the sediment composition is 72 wt% calcite, 22 wt% opal and 6 wt% barite with the sediment matrix consisting of 50% sediment and 50% interstitial fluid. Given the mean measured fluid composition (Table 1, Fluid 1) with $pO_2 = 10^{-1.65}$ atm (corresponding to O_2 in seawater at 3000 mbsf after Chester, 2000), and a temperature of 5°C, we assessed the possibility of precipitating iron oxi/hydroxides (hematite, goethite, magnetite), sulfates (gypsum, anhydrite, celestite and jarosite), and clay minerals (illite, muscovite, daphnite, clinochlore and glauconite). Smectites are entered in the model as 18 different pure phases.

Fig. 7 shows the fluid composition as a function of distance to the pyritic burrow, for different simulated durations. The fluid composition is modified by the oxidation of pyrite to a distance of 20-25 m after 1000 years. This distance increases to a maximum of about 40 m after 4000 years. We note that the chemical composition of pore fluids close to the burrow approachs a steady state after 4000 years. The pH decreases from 7.9 (initial pH in the sediment pore fluid) to 6.1 at the interface between pyrite and sediment after 4000 years. Fe and S increase from 5.7×10^{-16} to 1.1×10^{-13} mol/l and from $2.8.x\ 10^{-2}$ to $4.1.x\ 10^{-2}$ mol/l, respectively. Ca and C also increase from $1.2. \times 10^{-2}$ to 4.4×10^{-2} mol/l and from 1.8×10^{-3} to $6.6.10^{-2}$ mol/l respectively. Ba and Si slightly decrease from 8.4×10^{-8} to 6.2×10^{-8} mol/l and from 1.0×10^{-3} to 9.4×10^{-4} mol/l respectively. These chemical variations are related to mineralogical changes (Fig. 8). Pyrite oxidation induces a decrease in pH and a release of Fe and S to pore fluid. The dissolution of calcite buffers the system, limiting the pH decrease, and also leads to Ca and C concentration increases in solution. The calcium content in solution is lower than the carbonate content because the calcium is partially consumed by the precipitation of montmorillonite and gypsum. The silicon concentration also is dependent on two processes: dissolution of amorphous silica and precipitation of montmorillonite, as well as S that is released by pyrite oxidation and consumed by gypsum precipitation. However,

we observe that the mineralogical variations extend less than of the chemical modifications in the pore fluid.

The main mineralogical transformation occurs at the interface between pyrite and sediment. Fig. 9, which focuses on the first cell within the sediment, illustrates that the models predicts the dissolution of calcite and amorphous silica as soon as the pyrite dissolves. Calcite is completely dissolved after about 3500 years of reaction, whereas amorphous silica is entirely dissolved after about 2000 years. Barite remains stable during all simulation. The precipitation of montmorillonite is predicted from the start of reaction and the total amount progressively increases, up to 2 mol/l. Montmorillonite evolves from sodic to calcic. Another secondary phase that is predicted is the precipitation of gypsum, which occurs after 1000 years and reaches almost 4 mol/l after 4000 years.

4. DISCUSSION

4.1. Origin and stability conditions of pyrite

The mineralogical investigation and the modeling approach indicate that the formation of the scattered green grains within the calcareous oozes can be explained by two successive diagenetic redox conditions: a reducing stage with precipitation of pyrite and an oxidizing stage with progressive alteration of pyrite to iron-rich montmorillonite. These two stages are examined in detail below.

Framboidal pyrite is commonly described in marine sediments (e.g. Morse and Wang, 1997; Wilkin and Barnes, 1997; Butler and Rickard, 2000; Todorova et al., 2005; Dekov et al., 2007). Its formation is generally attributed to early diagenetic processes, resulting from microbial activity in natural environments, though abiotic synthesis is possible. The source of pyrite sulphur is almost entirely the result of sulphate reduction during microbial oxidation of organic matter in sediments (Berner, 1984). This reaction consumes and increases the alkalinity of the pore water following the generalized reaction: $2CHO + SO_4^{2-} = H_2S + 2HCO_3^{2-}$; H_2S produced by sulphate reduction may

react with Fe^{2+} leading to precipitation of aggregates of octahedra pyrite: $2H_2S + Fe^{2+} = FeS_2 + 2H^+$. Framboïdal pyrites occur in the inner part of the green grains that fill burrows in this study, suggesting oxidation-reduction conditions are suitable for pyrite stability (less than-180 mV, after Krauskopf, 1979 in Apello and Postma, 2005) that formed in microsites during decomposition of organic matter.

More oxidizing conditions prevailed in the surrounding bulk sediment, yielding to the alteration of pyrite. This scenario accounts for dissolution pits observed on pyrite surfaces. Whatever the reaction process, oxidation of pyrite generates an acidic, sulphur-rich solution that affects the release of transition metals to pore water (e.g. Blowes and Jambor, 1990; Eberling et al., 2000; Edwards et al., 2000; Jennings et al., 2000). In calcareous systems, carbonates can neutralize the acidity generated by pyrite oxidation. Buffering of fluid by carbonates, and formation of sulphates and iron oxi/hydroxides are often described, especially in context of acid mine drainage or in sedimentary rock outcrops (e.g. Andrews et al., 1996; Charpentier et al., 2001; Charpentier et al., 2004; Joeckel et al., 2005). Iron-oxide is the most common product of pyrite oxidation in soils or in marine sediments, however smectite is the main product of pyrite oxidation in these sediment (Gaudin et al., 2005). The present study confirms that, in certain conditions, pyrite is altered into smectite (iron-rich montmorillonite).

4.2. Conditions of iron-rich montmorillonite formation

In the Costa Rica margin sediment, clay particles surround the partially dissolved pyrites. Using EDX analyses on individual particles, an average structural formula was calculated by Gaudin et al. (2005): $[Si_{3.94}\ Al_{0.04}\ Fe_{0.02}\ O_{10}]\ (Fe_{1.42}\ Mg_{0.68}\ Mn_{0.02})\ (K_{0.11}\ Ca_{0.11}\ Na_{0.07}\ nH_2O)(OH)_2)$. X-Ray Diffraction analyses and IR spectroscopy data attested that the authigenic clay minerals are Fe^{3+}-rich dioctahedral smectite with a dominant octahedral charge (Gaudin et al., 2005). TEM observations and EDX analyses of the present study indicate that smectite grows from an

amorphous precursor that is the product of pyrite dissolution, and its formation implies the input of Si, O, Mg, K, Na and Ca to pore fluids.

We undertook a modeling approach in order to characterize conditions that allow the formation of a montmorillonite, consistent with that observed in the Costa Rica margin sediment. Modeling of pyrite oxidation by seawater at low temperatures in this environment predicts calcite and silica dissolution and the precipitation of clay minerals. Barite remains stable during each simulation, probably because barite is initially in equilibrium with respect to seawater and the increase in dissolved sulfate from pyrite oxidation further stabilizes barite. The simulated smectite structural formula ($[Si_4\ O_{10}]\ (Fe_{1.4}\ Mg_{0.6})\ (Na_{0.3}\ K_{0.1}\ Ca_{0.1})\ (OH)_2$) is close to that of the mean smectite formula obtained by chemical analyses. The consistency between experimental investigations and model results validates the thermodynamic data used in the calculation and the approach that we treated smectite as a solid solution. This study shows that iron-rich montmorillonite can be a product of pyrite oxidation by interaction with seawater in calcareous ooze at low temperature if silicon is available. The reaction described here is related to early diagenetic processes: local change of redox conditions in a closed system that is able to induce dissolution of pyrite and precipitation of smectite as a secondary product with amorphous Fe-rich phases as a precursor.

The formation of montmorillonite as the main product requires the presence of calcite at the contact with pyrite to buffer the system. Calcite also provides calcium to solution. Results of this study confirm that when the pH becomes acidic, iron oxi/hydroxides may dominate instead of montmorillonite. The oxidation of pyrite by seawater gives rise to acidic conditions, promoting the precipitation of Fe-oxides. This process is common in marine sediments. The thermodynamic modeling demonstrates that the presence of carbonate is essential to buffer the pH, allowing Fe-rich montmorillonite to precipitate. This result is consistent with experimental studies on smectite dissolution rates as a function of pH (Bauer and Berger, 1998, Golubev et al. 2006 and Rozalén et al., 2008). These authors showed that dissolution of smectite at 25°C occurs preferentially at pH <

6, indicating that smectites are more stable in neutral solutions.

4.3. Mechanism of iron-rich montmorillonite formation

TEM observations and analyses suggest that smectite grows from an amorphous precursor and its formation implies the input of Si, O, K, Na and Ca. However the dissolution of other mineral phases, such as siliceous fossils and silicates was not observed by Gaudin et al. (2005), but the evidence was probably too weak to be noticed.

A one-dimensional flow path approach was used to understand how smectite forms. A kinetic-rate law was used for pyrite oxidation, but for the other minerals a local equilibrium approximation was used. Given these parameters, duration and extent of reactions are only qualitative.

The main mineralogical transformations are predicted at or close to the interface between pyrite and sediment. Pyrite oxidation induces a decrease in pH and a release of Fe and S to the pore fluid. The pH is immediately buffered by calcite and amorphous silica. Silica, calcium and iron are mobilized by the precipitation of montmorillonite. The formation of iron-rich montmorillonite necessitates calcite and amorphous silica dissolution as well as pyrite oxidation. Gypsum precipitation is also predicted after 1000 years in large amounts because S increases in solution. Gypsum has been observed only as a trace mineral in the studied sediment. Simulations may underestimate the time that it takes to form gypsum because of the local equilibrium approximation. Even if the sediment is more than 2 Ma old, its diagenetic maturity may correspond to about 1000 years modeled.

4.4. Iron-rich montmorillonite as glauconite precursor?

Green grains of glaucony are commonly formed in marine environments with a low

sedimentation rate (Amorosi, 1997). These grains are a mixture of Fe-rich smectite and glauconite minerals. The formation of glauconite is described as a transformation process from a iron-rich montmorillonite precursor (Meunier, 2003): iron-rich montmorillonite would be an intermediate mineral phase whose persistence would be not only be controlled by chemical and thermal conditions (very low temperature) but also by kinetic reactions. Odin and Matter (1981) suggested that the degree of evolution of the glauconitization process depends on the residence time of the green grains at the seafloor before burial. The maturity of glaucony grains are based on their chemistry with higher K_2O content evolving from a smectitic precursor to a K-rich glauconite mica (Amorosi, 1997). The seawater depth is also an important factor according to Odin and Morton (1988) and Wiewióra et al. (2001). These authors suggest that glauconitization can be effective at 60-500 m water depth, because at greater water depths, this process is inhibited by low temperature and low sedimentation rates. Meunier and El Albani (2007) recently illustrated that the glauconitization processes depends on the nature of the sediment and its porosity. In the present study, we suggest that the formation of authigenic iron-rich montmorillonite is related to early diagenetic processes in deep-water sediments (3000 m). The absence of glauconite-mica like particles in the green grains sampled in the Costa Rica margin sediments suggest that the precipitation of iron-rich montmorillonite in this environment may correspond to the first step of an overall glauconitization process, including iron-rich montmorillonite-to-glauconite conversion via glauconite-smectite mixed layer minerals (Gaudin et al., 2005). However, our model simulations indicate that for conditions within Costa Rica margin sediments ($pCO_2 = 10^{-3.48}$atm, $pO_2 = 10^{-1.65}$atm and a temperature of 5°C, interstitial fluid deriving from seawater), the iron-rich montmorillonite remains stable. The present study demonstrates that the formation of glauconite is also controlled by the composition of the sediment. In the Costa Rica margin sediment, the absence of aluminum could explain why the formation of glauconite is hindered and not observed.

5. CONCLUSIONS

An iron-rich montmorillonite is widespread in pelagic calcareous sediments from the Costa Rica margin. Using a detailed mineralogical study by TEM of microtomed samples combined with model simulations of pore fluid-sediment interactions, we constrain the conditions and mechanism for the formation of this iron-rich montmorillonite.

1) We demonstrate that geochemical modeling can be used to test and validate hypotheses based on reaction conditions that include smectite solid solutions, even if measured thermodynamic data are lacking.

2) iron-rich montmorillonites are rarely described in marine environments, and montmorillonites are generally thought to contain Al. EDX analyses confirm the presence of an iron-rich, aluminum-free montmorillonite in millimeter- to centimeter-long green grains. Green grains showed a concentric zoning with a black core consisting of partially dissolved pyrite. Pyrite grains are surrounded by montmorillonite that grows from an amorphous precursor.

3) This iron-rich montmorillonite is the product of pyrite oxidation by interaction with pore fluid under very specific conditions and the order is important. First, the formation of pyrites in microsites implies reducing conditions resulting from microbial consumption of organic matter. This stage is followed by pyrite alteration with prevailing oxidizing conditions at neutral pH. Pyrite should be in close contact with calcareous sediment, otherwise the pH becomes acidic and iron oxides precipitate instead of clays. Thus, iron-rich montmorillonite formation requires inputs of Si, O, Mg, K, Na and Ca. The sediment must be a source of silica (e.g., amorphous silica) but no aluminum phases are necessary.

4) Glauconite is not found as a product of iron-rich montmorillonite in the specific modeling conditions. The very low content of aluminum in the pelagic calcareous sediment suggests that glauconite formation is controlled by the chemistry of the sediment.

REFERENCES

Amorosi A. (1997) Detecting compositional, spatial, and temporal attributes of glaucony: a tool for provenance research, *Sediment. Geol.* **109**, 135-153.

Apello C. A. J. and Postma D. (2005) *Geochemistry, groundwater and pollution*. Balkema Publishers, Amsterdam, the Netherlands.

Andrews J. E., Brimblecombe P., Jickells T. D. and Liss P. S. (1996) *An Introduction to Environmental Chemistry*. Blackwell, Oxford.

Bauer A. and Berger G. (1998) Kaolinite and smectite dissolution rate in high molar KOH solutions at 35°C and 80°C. *Appl. Geochem.* **13**, 905-916.

Berner R. A. (1984) Sedimentary pyrite formation: An update. *Geochim. Cosmochim. Acta* **48**, 605-615.

Bischoff J. L. (1972) A ferroan nontronite from the Red Sea geothermal system. *Clays Clay Miner.* **20**, 217-223.

Blowes D. W. and Jambor J. L. (1990) The pore-water geochemistry and the mineralogy of the vadose zone of sulfide tailings, Waite Amulet, Quebec, Canada. *Appl. Geochem.* **5**, 327-346.

Buatier M. D., Honnorez J. and Ehret G. (1989) Fe-smectite-glauconite transition in hydrothermal clays from GSC. *Clays Clay Miner.* **37**, 532-541.

Buatier M. D., Karpoff A.M. and Charpentier D. (2002) Clays and zeolite authigenesis in sediments from the flank of the Juan de Fuca ridge. *Clay Miner.* **37**, 143-155.

Buatier M. D., Ouyang K. and Sanchez J. P. (1993) Iron in hydrothermal clays from the galapagos spreading centre mounds: consequences for the clay transition mechanism. *Clay Miner.* **28**, 641-655.

Butler I. B. and Rickard D. (2000) Framboidal pyrite formation via the oxidation of iron (II) monosulphide by hydrogen sulphide. *Geochim. Cosmochim. Acta* **64**, 2665-2672.

Charpentier D., Cathelineau M., Mosser-Ruck R. and Bruno G. (2001) Evolution minéralogique des argilites en zones sous-saturées oxydées : exemple des parois du tunnel de Tournemire (Aveyron, France). *Cr. Acad. Sci. II A* **332**, 601-607.

Charpentier D., Mosser-Ruck R., Cathelineau M. and Guillaume D. (2004) Oxidation of mudstone in a tunnel (Tournemire, France): consequences on mineralogy and crystal chemistry of clay minerals. *Clay Miner*. **39**, 135-149.

Chen S. Y., Ambe S., Takematsu N. and Ambe F. (1996) The chemical states of iron in marine sediments by means of Mössbauer spectroscopy in combination with chemical leachings. *J. Oceanogr.* **52**, 705-715.

Chermak J. A. and Rimstidt J. D. (1989) Estimating the thermodynamic properties (ΔGf° and ΔHf°) of silicates minerals at 298K from the sum of polyedral contributions. *Am. Mineral.* **74**, 1023-1031.

Chermak J. A. and Rimstidt J. D. (1990) Estimating the free energy of formation of silicates minerals at high temperature from the sum of polyedral contributions. *Am. Mineral.* **75**, 1376-1380.

Chester R. (2000) *Marine Geochemistry*. Blackwell Science Ltd.

Cole T. G. and Shaw H. F. (1983) The nature and origin of authigenic smectites in some recent sediments. *Clay Miner.* **18**, 239-252.

Corliss J. B., Lyle M. and Dymond J. (1978) The chemistry of hydrothermal mounds near the Galapagos Rift. *Earth Planet. Sci. Lett.* **40**, 12–24.

Dekov V. M., Scholten J. C., Botz R., Garbe-Schönberg C.D. and Stoffers P. (2007) Fe-Mn-(hydr)oxide-carbonate crusts from the Kebrit Deep, Red Sea: Precipitation at the seawater/brine redoxcline. *Mar. Geol.* **236**, 95-119.

Elberling B., Schippers A. and Sand W. (2000) Bacterial and chemical oxidation of pyritic mine tailings at low temperatures. *J. Contam. Hydrol.* **41**, 225-238.

Edwards K. J., Bond P. L., Druschel G. K., McGuire M. M., Hamers R. J. and Banfield J. F. (2000) Geochemical and biological aspects of sulfide mineral dissolution: lessons from Iron Mountain, California. *Chem. Geol.* **169**, 383-397.

Elsass F., Beaumont A., Pernes M., Jaunet A.M. and Tessier D. (1988) Changes in layer organization of Na and Ca exchanged smectite during solvent exchange for embedment in resin. *Can. Miner*. **36**, 1325-1333.

Faure G. (1991) *Principles and applications of inorganic geochemistry*. Macmillan Publishing Compagny, New York.

Garrels R. M. and Thompson M. E. (1960) Oxidation of pyrite by iron sulfate solutions. *Am. J. Sci.* **258A**, 57-67.

Gaudin A., Buatier M. D., Beaufort D., Petit S., Grauby O. and Decareau A. (2005) Characterization and origin of Fe^{3+}-Montmorillonite in deep water calcareous sediments (Pacific ocean, Costa Rica margin). *Clays Clay Miner.* **53**, 452-465.

Giresse P. and Wiewióra A. (2001) Stratigraphic condensed deposition and diagenetic evolution of green clay minerals in deep water sediments on the Ivory Coast-Ghana Ridge. *Mar. Geol.* **179**, 51-70.

Golubev S. V., Bauer A. and Pokrovsky O. S. (2006) Effect of pH and organic ligands on the kinetics of smectite dissolution at 25 °C. *Geochim. Cosmochim. Acta* **70**, 4436-4451.

Jennings S. R., Dollhopf D. J. and Inskeep W. P. (2000) Acid production from sulfide minerals using hydrogen peroxide weathering. *Appl. Geochem*. **15**, 247-255.

Joeckel R. M., Clement B. J. and VanFleet Bates L. R. (2005) Sulfate-mineral crusts from pyrite weathering and acid rock drainage in the Dakota Formation and Graneros Shale, Jefferson County, Nebraska. *Chem. Geol*. **215**, 433– 452.

Johnson J. W., Oelkers E. H. and Helgeson H. C. (1992) SUPCRT92: Software pachage for calculating the standard molal thermodynamic properties of minerals gases, aqueous species and reaction among them as functions of temperature and pressure. *Comput. Geol.* **18**, 899-947.

Kimura, G., Silver, E.A., Blum, P., et al., 1997. *Proc. ODP, Init. Repts.*, 170: College Station, TX (Ocean Drilling Program). doi:10.2973/odp.proc.ir.170.1997

Köhler B., Singer A. and Stoffers P. (1994) Biogenic nontronite from marine white smoker

chimneys. *Clays Clay Miner.* **42**, 689–701.

Krauskopf K.B. (1979) *Introduction to geochemistry*. MCGraw-Hill, New York.

Meunier A. (2003) *Argiles.* Société géologique de France, GB Science Publisher, France.

Meunier A. and El Albani A. (2007) The glauconite-Fe-illite-Fe-smectite problem: a critical review. *Terra Nova*, **19**, 95-104.

Moorby S. A. and Cronan D. S. (1983) The geochemistry of hydrothermal and pelagic sediments from the Galapagos hydrothermal mounds field. DSDP Leg 70, *Miner. Mag.*, **47**, 291-300.

Morse J. W. and Wang Q. (1997) Pyrite formation under conditions approximating those in anoxic sediments: II. Influence of precursor iron minerals and organic matter. *Mar. Geol.* **57**, 187-193.

Odin G. S. and Matter A. (1981) De glauconiarium originae. *Sedimentology* **28**, 614-641.

Odin G. S. and Morton A. C. (1988) Authigenic green particles from marine environments. In *Developments in sedimentology* (eds. G. V. Chilingarian and K. H. Wolf). Elsevier, Amsterdam. pp. 213-264.

Panin V. V., Karavaiko G. I. and Pol'kin S. I. (1985) Mechanism and kinetics of bacterial oxidation of suphide minerals. In *Biogeotechnology of metals* (eds. G. I. Karavaiko and S. N. Groudev). UNEP Moscow URSS. pp. 197-215.

Parkhurst D. L. and Appelo C. A. J. (1999) *User's guide to PHREEQC (Version 2) - a computer program for speciation, reaction-path, advective-transport, and inverse geochemical calculations.* U.S. Geological Survey Water-Resources Investigations Report, 99-4259.

Parkhurst D. L. (1995) *User's guide to PHREEQC - a computer program for speciation, reaction-path, advective-transport, and inverse geochemical calculations.* U.S. Geological Survey Water-Resources Investigations Report, 95-4227.

Rozalén M. L., Huertas F. J., Brady P. V., Cama J., Garcıá-Palma S. and Linares J. (2008) Experimental study of the effect of pH on the kinetics of montmorillonite dissolution at 25°C. *Geochim. Cosmochim. Acta* **72**, 4224-4253.

Sánchez España J. (2007) The behavior of Iron and Aluminum in acid mine drainage. Speciation,

mineralogy, and environmental significance. In *Thermodynamics, Solubility and Environmental Issues* (ed T.M. Letcher).Elsevier B.V.. pp. 137-150.

Sévèque J.L. (1986) Etude expérimentale de la dissolution des minéraux sulfurés en milieu oxydant : application à la prospection minière. Ph. D. thesis, Univ. Paris VI.

Singer A., Stoffers P., Heller-Kallai L. and Szafranek D. (1984) Nontronite in a deep-sea core from the South Pacific. *Clays Clay Miner*. **32**, 375–383.

Silver, E.A., Kimura, G., and Shipley, T.H. (Eds.), 2001. *Proc. ODP, Sci. Results,* 170: College Station, TX (Ocean Drilling Program). doi:10.2973/odp.proc.sr.170.2001

Spinnelli G. A. and Underwood M. B. (2004) Character of sediments entering the Costa Rica subduction zone: Implications for partitioning of water along the plate interface. *Isl. Arc* **13**, 432-451.

Stefánsson A., Arnórsson S. and Sveinbjörnsdóttir A. E. (2005) Redox reactions and potentials in natural waters at disequilibrium. *Chem. Geol.* **221**, 289-311.

Tessier D. (1984) Hydratation, gonflement et structuration des matériaux argileux au cours de la dessication et de la réhumectation. Ph. D. thesis, Université de Paris & INRA Versailles, France.

Thompson G., Mottl M. and. Rona P. A. (1985) Morphology, mineralogy and chemistry of hydrothermal deposits from the TAG area, 26° N Mid-Atlantic Ridge. *Chem. Geol.* **49**, 243–257.

Todorova S. G., Siegel D. I. and Costello A. M. (2005) Microbial Fe(III) reduction in a minerotrophic wetland – geochemical controls and involvment in organic matter decomposition. *Appl. Geochem*. 20, 1120-1130.

Wheat, C. G., and A. T. Fisher (2008), Massive, low-temperature hydrothermal flow from a basaltic outcrop on 23 Ma seafloor of the Cocos Plate: Chemical constraints and implications, *Geochem. Geophys. Geosyst.*, 9, Q12O14, doi:10.1029/2008GC002136

Wiewióra A., Giresse P., Petit S. and Wilamowski A. (2001) A deep-water glauconitization process on the Ivory Coast-Ghana marginal ridge (ODP site 959): determination of Fe3+-rich montmorillonite in green grains. *Clays Clay Miner*. **49**, 540-558.

Williamson M. A. and Rimstidt J. D. (1994) The kinetics and electrochemical rate-determining step of aqueous pyrite oxidation. *Geochim. Cosmochim. Acta* **58**, 5443-5454.

Wilkin R. T. and Barnes H. L. (1997) Formation processes of framboidal pyrite. *Geochim. Cosmochim. Acta* **61**, 323-339.

Wolery T. J. and Daveler S. A. (1992) *EQ6, a computer program for reaction path modelling of aqueous geochemical systems: user's guide and documentation*. Lawrence Livermore National Laboratory, University of California.

Wolery T. J. (1992) *EQ3NR, a computer program for geological aqueous speciation-solubility calculations: theoritical manual, user's guide and related documentation*. Lawrence Livermore National Laboratory, University of California.

TABLES

Table 1. Mean pore fluid composition (1), example of seawater composition from Faure (1991) (2) and interstitial fluid obtained by modeling seawater equilibration with sediment (3). Comparison with the mean analysed interstitial fluid composition (4).

	mmol/kg							*µmol/kg*				
	pH	Cl	S	Na	Ca	Mg	K	*Si*	Fe	Sr	Ba	B
Mean pore fluid (1)	7.65	548.0	27.7	461	11.4	52.5	10.3	470	1.120	88.9	0.14	436
Sea water from Faure (1991) (2)	-	550.0	28.1	470	10.3	53.1	10.2	*100*	0.001	86.7	0.10	416
Modelled interstitial fluid (3)	7.94	550.0	28.1	470	10.4	53.1	10.2	1050	0.001	86.7	0.08	416
Analyzed/Simulated (4)	0.96	1.00	0.99	0.98	1.09	0.99	1.01	0.45	1018.18	1.02	1.68	1.05

Table 2. Molal Gibbs energy of formation of oxi/hydroxides calculated at 5°C using equations given by Chermack and Rimstidt (1990) except for $Fe(OH)_3$[6] calculated from Chermack and Rimstidt (1989).

Oxi/hydroxides	G ($kJ.mol^{-1}$)
Al_2O_3 [4]	-1637.0
Al_2O_3 [6]	-1600.9
$Al(OH)_3$ [6]	-1190.9
SiO_2 [4]	-857.8
MgO [6]	-631.0
$Mg(OH)_2$ [6]	-857.8
CaO [8-z]	-711.8
Na_2O [6-8]	-673.2
K_2O [8-12]	-723.7
FeO [6]	-285.5
$Fe(OH)_2$ [6]	-545.7
Fe_2O_3 [6]	-787.0
$Fe(OH)_3$ [6]	-734.0

Table 3. Composition, ΔG of formation, ΔG of reaction and log(K) of smectites and glauconite added to the data base. Thermodynamical constants have been calculated at 5°C using Supcrt and Table 1 data.

	Si	Al	Fe	Mg	Na	K	Ca	O	OH	ΔG_f J mol^{-1}	ΔG_r J mol^{-1}	Log(K)
K mtmor Fe HC	4	0	1.33	0.67	0	0.67	0	10	2	-4850000	16500	-2.89
Na mtmor Fe HC	4	0	1.33	0.67	0.67	0	0	10	2	-4830000	12900	-2.25
Ca mtmor Fe HC	4	0	1.33	0.67	0	0	0.335	10	2	-4840000	15100	-2.65
K mtmor Fe BC	4	0	1.67	0.33	0	0.33	0	10	2	-4640000	55900	-9.79
Na mtmor Fe BC	4	0	1.67	0.33	0.33	0	0	10	2	-4630000	54100	-9.48
Ca mtmor Fe BC	4	0	1.67	0.33	0	0	0.165	10	2	-4640000	55200	-9.67
K saponite Fe	3.67	0.33	3	0	0	0.33	0	10	2	-4650000	-67800	11.88
Na saponite Fe	3.67	0.33	3	0	0.33	0	0	10	2	-4650000	-69600	12.19
Ca saponite Fe	3.67	0.33	3	0	0	0	0.165	10	2	-4650000	-68500	12.00
K saponite Mg	3.67	0.33	0	3	0	0.33	0	10	2	-5660000	-155000	27.15
Na saponite Mg	3.67	0.33	0	3	0.33	0	0	10	2	-5650000	-157000	27.46
Ca saponite Mg	3.67	0.33	0	3	0	0	0.165	10	2	-5660000	-156000	27.27
K mtmor Al HC	4	1.33	0	0.67	0	0.67	0	10	2	-5410000	-37700	6.61
Na mtmor Al HC	4	1.33	0	0.67	0.67	0	0	10	2	-5400000	-41400	7.25
Ca mtmor Al HC	4	1.33	0	0.67	0	0	0.335	10	2	-5410000	-39100	6.85
K mtmor Al BC	4	1.67	0	0.33	0	0.33	0	10	2	-5350000	-14100	2.47
Na mtmor Al BC	4	1.67	0	0.33	0.33	0	0	10	2	-5340000	-15900	2.79
Ca mtmor Al BC	4	1.67	0	0.33	0	0	0.165	10	2	-5350000	-14800	2.59
Glauconite	3.67	0.33	1.33	0.67	0	1	0	10	2	-4950000	-13200	2.31

FIGURES

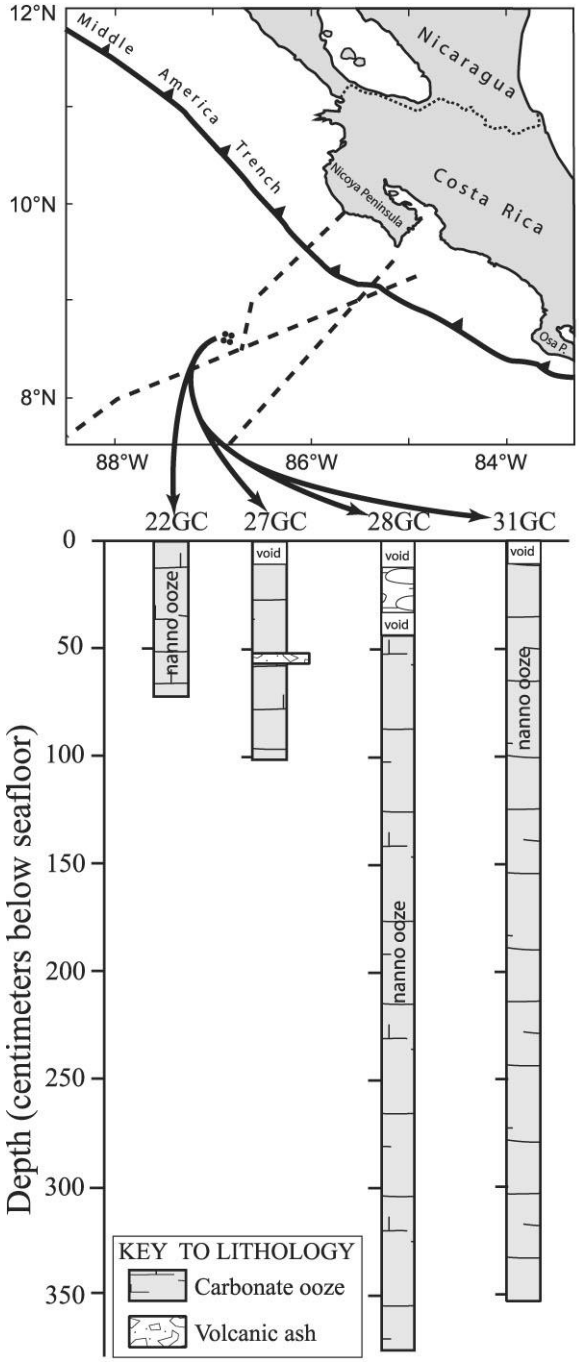

Fig. 1. Location of the studied samples and schematic presentation of the studied cores (modified from Gaudin et al., 2005).

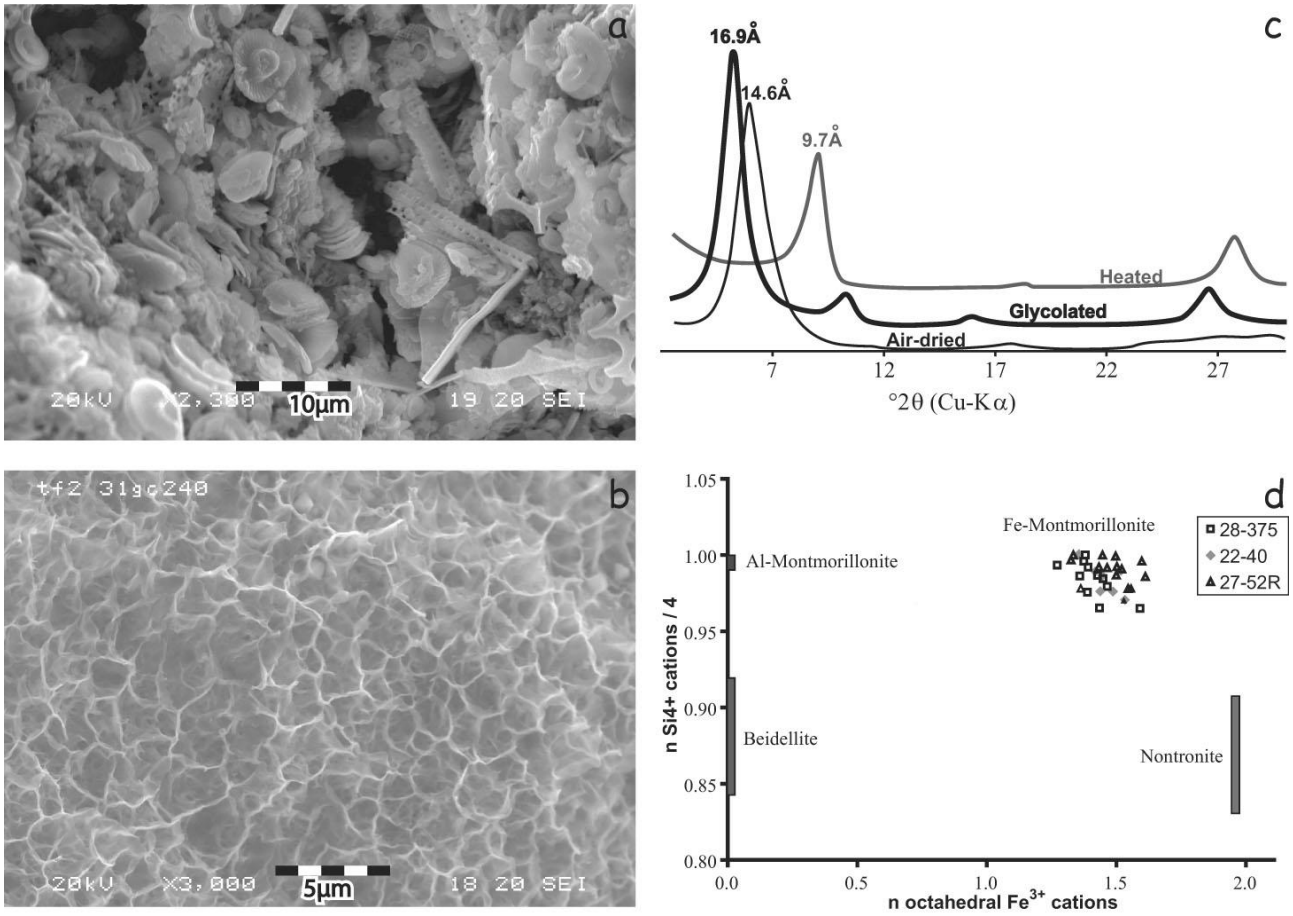

Fig. 2. Synthesis of mineralogical results (modified from Gaudin et al., 2005). SEM images a) of the carbonated biogenic ooze (sample 31GC-13) and b) of green rim composed of smectites (sample 31GC-240). c) XRD patterns of oriented Ca^{2+}-saturated smectite preparations (<2µm fraction) air-dried, glycolated and heated (sample 27GC-52). d) TEM-EDX analyses of Ca^{2+}-saturated smectite particles reported in the 4Si-Σ^{VI}Fe diagram (modified from Meunier, 2003).

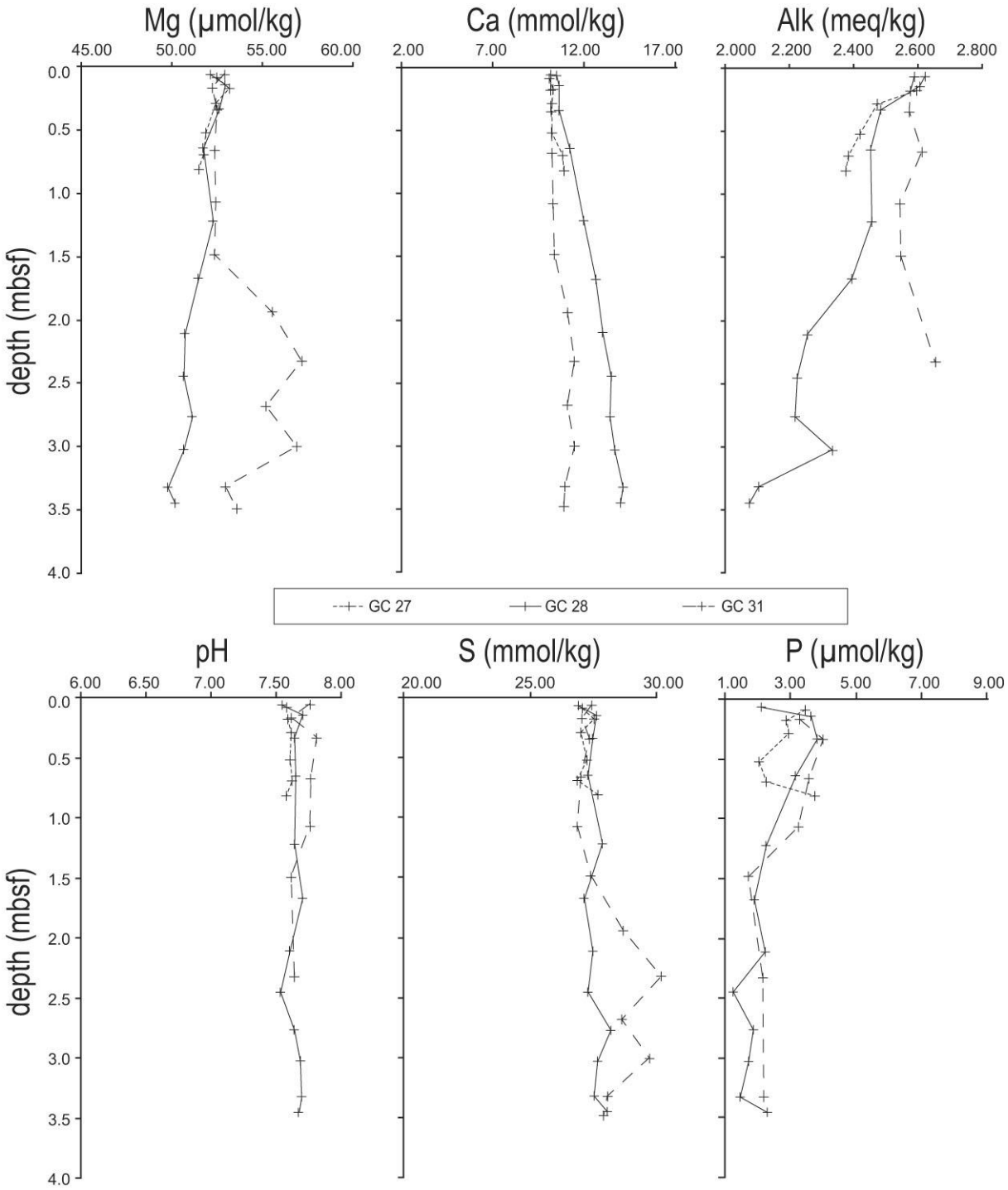

Fig. 3. Chemical composition (Mg, Ca, alkalinity, pH, sulphate and phosphate) of pore waters from three sediment cores west of the Costa Rica Margin where green clays were sampled.

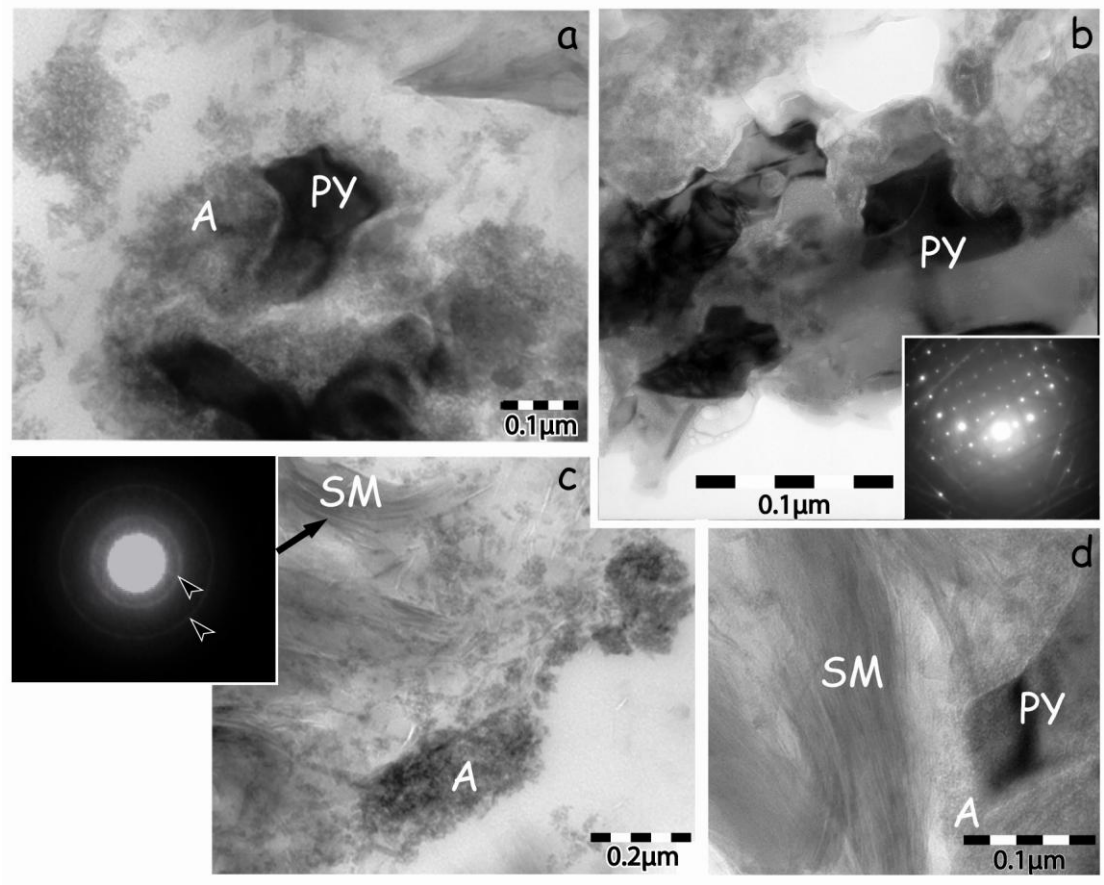

Fig. 4. Transmission electron microscopy (TEM) images and selected area electron diffraction (SAED) patterns of impregnated green grains showing dissolution of pyrite (PY) and newly formed amorphous particles (A) and smectite (SM). a) aggregates of nano-sized amorphous particles surrounding partially dissolved pyrite grains. b) detailed image of partially dissolved pyrite grain and its SAED pattern. c) amorphous phases in contact with smectite particles and SAED pattern on smectite (two diffraction rings, respectively at 4.5 and 2.6 Å). d) general view of the three major components of the green grains (pyrite, amorphous particles and smectite particles of more than 10 stacking layers).

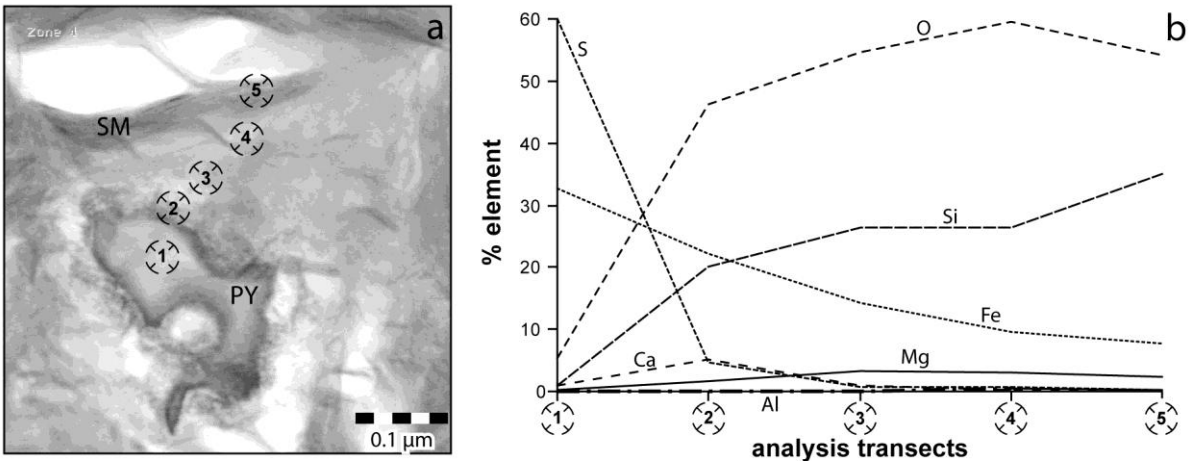

Fig. 5. Evolution of the chemical composition of amorphous to smectite particles near a pyrite grain. a. STEM image of the analysed profile (SM : smectite, PY : Pyrite, numbers indicate the position of AEM analysis). b. AEM analyses along the transect illustrated in STEM image.

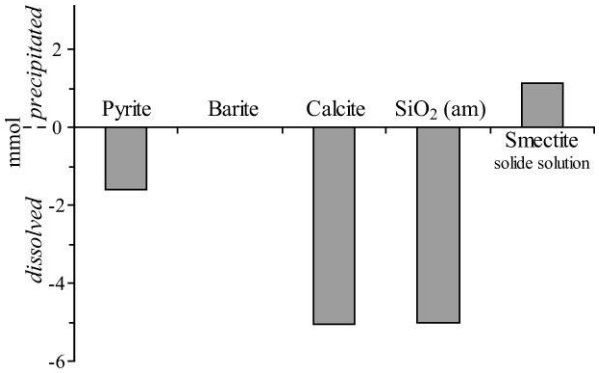

Fig. 6. Model simulations of batch interactions between the interstitial fluid and sediment + pyrite: to reach equilibrium, pyrite, calcite and SiO_2 (am) should dissolved whereas smectite solid solution precipitates.

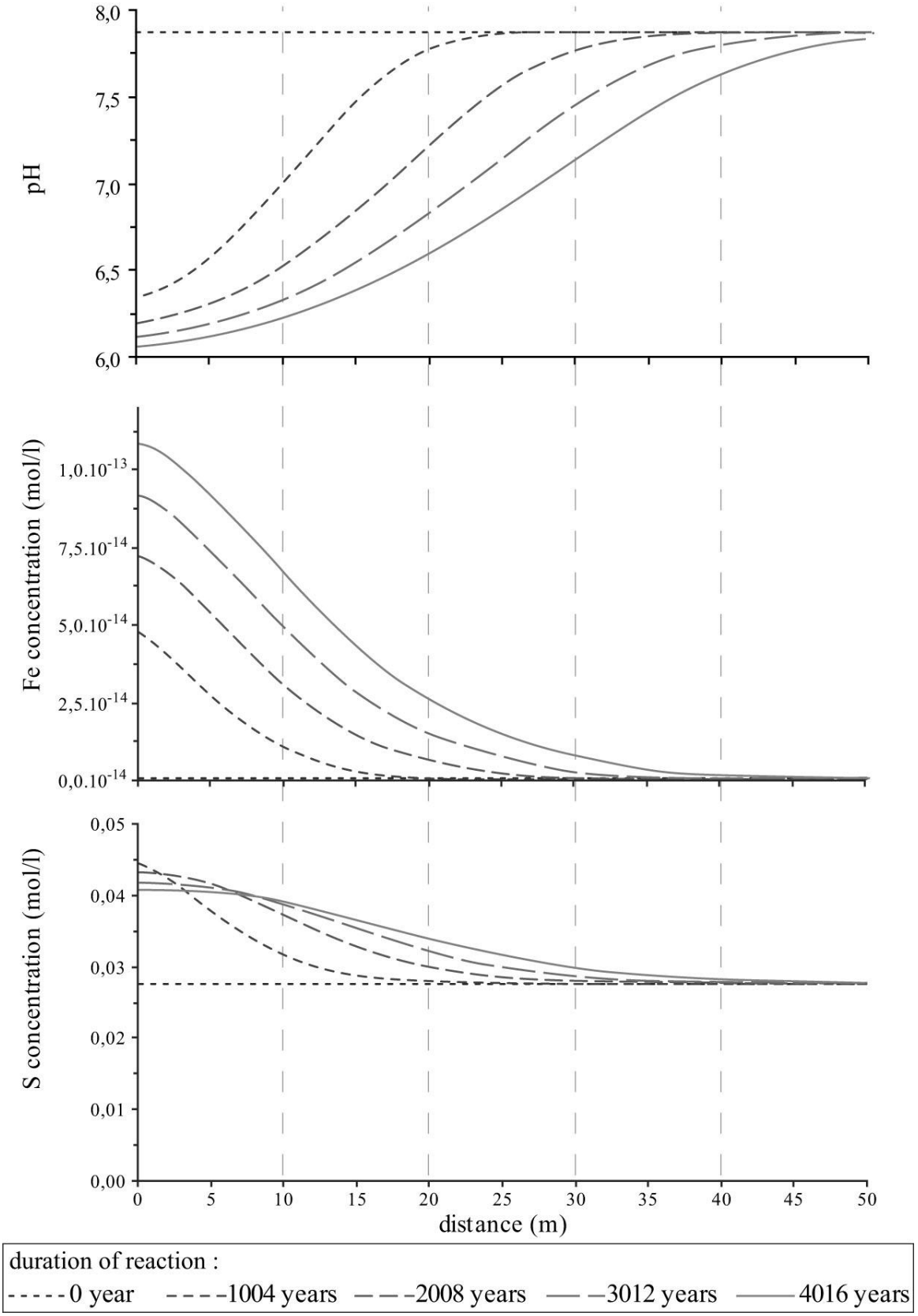

Fig. 7. Predicted chemical composition using PhreeqC of interstitial fluid as a function of distance to the pyritic burrow for 1004, 2008, 3012 and 4016 years of reaction. Aqueous components are transported by diffusion.

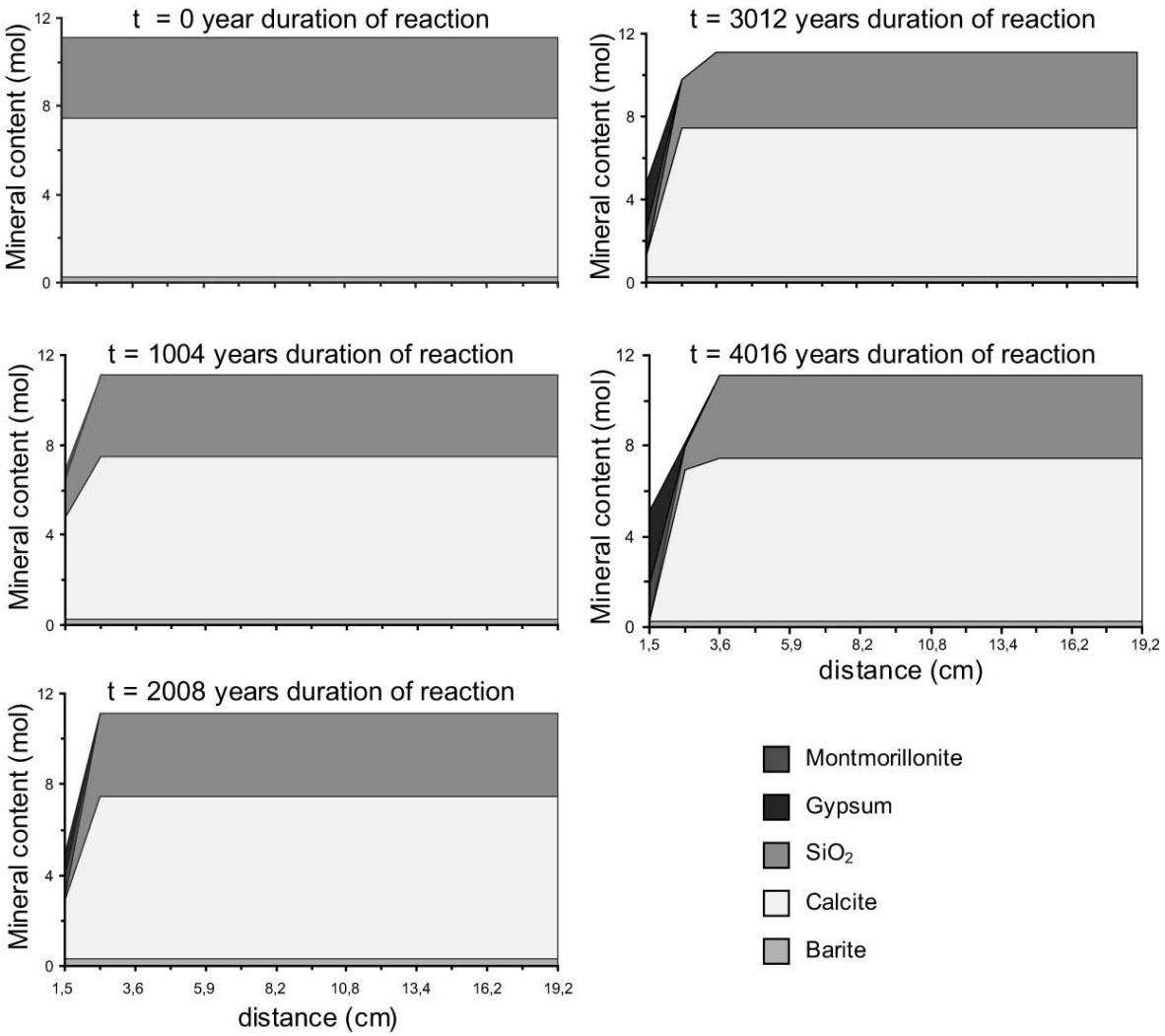

Fig. 8. Predicted mineralogical composition using PhreeqC of the sediment as a function of distance to the pyritic burrow for 1004, 2008, 3012 and 4016 years of reaction.

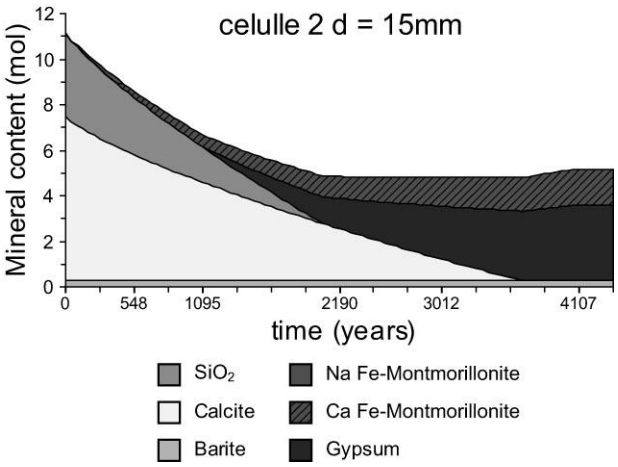

Fig. 9. Composition of the sediment at the interface with pyrite predicted by PhreeqC as a function of time.

FIGURE CAPTIONS

Fig. 1. Location of the studied samples and schematic presentation of the studied cores (modified from Gaudin et al., 2005).

Fig. 2. Synthesis of mineralogical results (modified from Gaudin et al., 2005). SEM images a) of the carbonated biogenic ooze (sample 31GC-13) and b) of green rim composed of smectites (sample 31GC-240). c) XRD patterns of oriented Ca^{2+}-saturated smectite preparations (<2µm fraction) air-dried, glycolated and heated (sample 27GC-52). d) TEM-EDX analyses of Ca^{2+}-saturated smectite particles reported in the $4Si\text{-}\Sigma^{VI}Fe$ diagram (modified from Meunier, 2003).

Fig. 3. Chemical composition (Mg, Ca, alkalinity, pH, sulphate and phosphate) of pore waters from three sediment cores west of the Costa Rica Margin where green clays were sampled.

Fig. 4. Transmission electron microscopy (TEM) images and selected area electron diffraction (SAED) patterns of impregnated green grains showing dissolution of pyrite (PY) and newly formed amorphous particles (A) and smectite (SM). a) aggregates of nano-sized amorphous particles surrounding partially dissolved pyrite grains. b) detailed image of partially dissolved pyrite grain and its SAED pattern. c) amorphous phases in contact with smectite particles and SAED pattern on smectite (two diffraction rings, respectively at 4.5 and 2.6 Å). d) general view of the three major components of the green grains (pyrite, amorphous particles and smectite particles of more than 10 stacking layers).

Fig. 5. Evolution of the chemical composition of amorphous to smectite particles near a pyrite

grain. a. STEM image of the analysed profile (SM : smectite, PY : Pyrite, numbers indicate the position of AEM analysis). b. AEM analyses along the transect illustrated in STEM image.

Fig. 6. Model simulations of batch interactions between the interstitial fluid and sediment + pyrite: to reach equilibrium, pyrite, calcite and SiO_2 (am) should dissolved whereas smectite solid solution precipitates.

Fig. 7. Predicted chemical composition using PhreeqC of interstitial fluid as a function of distance to the pyritic burrow for 1004, 2008, 3012 and 4016 years of reaction. Aqueous components are transported by diffusion.

Fig. 8. Predicted mineralogical composition using PhreeqC of the sediment as a function of distance to the pyritic burrow for 1004, 2008, 3012 and 4016 years of reaction.

Fig. 9. Composition of the sediment at the interface with pyrite predicted by PhreeqC as a function of time.